

Hybrid models for simulating blood flow in microvascular networks

E. Vidotto¹, T. Koch², T. Köppl¹, R. Helmig², B. Wohlmuth¹

Key words: microcirculation, homogenization, mixed-dimension models, multiscale models, hybrid models

Mathematics Subject Classification: 76S05, 76Z05, 92C10, 92B99

Abstract

In this paper, we are concerned with the simulation of blood flow in microvascular networks and the surrounding tissue. To reduce the computational complexity of this issue, the network structures are modeled by a one-dimensional graph, whose location in space is determined by the centerlines of the three-dimensional vessels. The surrounding tissue is considered as a homogeneous porous medium. Darcy's equation is used to simulate flow in the extra-vascular space, where the mass exchange with the blood vessels is accounted for by means of line source terms. However, this model reduction approach still causes high computational costs, in particular, when larger parts of an organ have to be simulated. This observation motivates the consideration of a further model reduction step. Thereby, we homogenize the fine scale structures of the microvascular networks resulting in a new hybrid approach modeling the fine scale structures as a heterogeneous porous medium and the flow in the larger vessels by one-dimensional flow equations. Both modeling approaches are compared with respect to mass fluxes and averaged pressures. The simulations have been performed on a microvascular network that has been extracted from the cortex of a rat brain.

1 Introduction

Modeling of blood flow and transport at the level of microcirculation is an interesting subfield in biomedical engineering. A reliable computational model for the microcirculation of the human body would enable physicians and pharmacists to obtain better insight into the oxygen supply of cells, the waste removal from the interstitial space [25] and further important biological processes without the need to perform expensive and risky experiments [6, 9, 41]. Besides, such models open up the possibility to study the impact of diseases like Alzheimer's

¹Department of Mathematics, University of Technology Munich, Boltzmannstr. 3, 85748 Garching bei München, Germany, vidotto@ma.tum.de, koepplto@ma.tum.de, wohlmuth@ma.tum.de

²Department of Hydromechanics and Modelling of Hydrosystems, University of Stuttgart, Pfaffenwaldring 61, 70569 Stuttgart, Germany timo.koch@iws.uni-stuttgart.de, rainer.helmig@iws.uni-stuttgart.de

[27] and to improve medicines and therapies for cancer treatment [8, 26, 34, 36]. Well known therapies for cancer treatment are, e.g., hyperthermia [39, 54] or the injection of therapeutic agents preventing the vascularization of cancer tissue [50]. In order to increase the efficiency of the mentioned cancer therapies, it is crucial to focus the therapeutic agents or the heat on the cancerous part of an affected organ while maintaining the rest of the tissue. In order to be able to simulate the distribution of heat and the concentration of therapeutic agents with an adequate accuracy, the hierarchical structure of the vascular system supplying the considered organ has to be taken into account.

However, even for vascular systems contained in small volumes covering just a few cubic millimetres, it is a challenging task to simulate flow in the microvascular networks and the interstitial space, since the flow in a complex network structure consisting of thousands of vessels [19] (Chap. 1) is coupled with the flow in the surrounding tissue matrix [13, 43].

As a consequence, several model reduction techniques have been developed for simulating flow through an entire organ or parts of an organ. A widespread technique in this field are homogenization techniques. Thereby brain tissue and the vascular system are considered as two different continua modeled as porous media [15, 38, 47, 48] and the pressure and velocity field are computed by means of Darcy's equation [24, 28]. Using this approach, the computational effort and the data volume are significantly reduced. On the other hand, both the pressure and the velocity field can only be described in an averaged sense, neglecting the exact structure of the vascular system. As a result, the distribution of therapeutic agents or heat might not be computed with sufficient accuracy. A further challenge is to determine suitable permeability tensors for the Darcy equation reflecting the structure of the vascular trees in an averaged way. Thereby brain tissue and the vascular system are considered as two different continua modeled as porous media [15, 38, 47, 48] and the pressure and velocity field are computed by means of Darcy's equation [24, 28, 52, 38].

Another way to decrease the computational complexity, is to describe the vascular networks by means of one-dimensional (1D) flow models [11, 53, 36, 20, 44, 22], while the surrounding tissue is considered as a three-dimensional porous medium. By this, an expensive meshing of a three-dimensional (3D) blood vessel system is avoided and at the same time the hierarchical structure of the vascular system is maintained. However, elaborate concepts for coupling one-dimensional flow equations with a flow equation (Darcy equation) for a three-dimensional flow problem [10, 31, 30] have to be developed. This is done by constructing suitable source terms for both the Darcy equation in 3D and the 1D flow problems. On closer examination, one notes that the source term in 3D consists of Dirac measures concentrated on the centerline of the vessels or the corresponding vessel walls, inducing a certain roughness into the solution of the 3D Darcy equation. Due to possible singularities or kinks occurring in the solution sufficiently fine meshes are required to obtain an accurate numerical solution.

Here, we propose a new hybrid approach which preserves the advantages of reduced order models, while preserving a sufficiently high accuracy. The idea is to model the larger vessels by 1D flow models, whereas the capillaries and tissue are considered as porous continua, as it is done in the homogenization approach. We apply this hybrid modeling approach to a microvascular system filling a volume of $1.134 \text{ mm} \times 1.134 \text{ mm} \times 2.268 \text{ mm}$ (see Fig. 1). This microvascular system was taken from the brain of a rat and the corresponding

data was generated by the group of B. Weber (University of Zurich) [45]. Within this network, one can find several penetrating arterioles and venules connecting this vascular subsystem to the macrocirculation of the rat’s brain, see Fig. 1. Our motivation to choose this approach is that by resolving the largest vessels in this volume, the main hierarchy of the vessel system is incorporated into the model. Moreover, using a homogenized double continuum model for the capillaries and the tissue, we have a less complex model which will certainly yield some speed-up, if several units of cubes of a few cubic millimetres are aggregated to simulate larger parts of an organ. Compared to other works [16, 40, 49] investigating hybrid approaches for microvascular systems, we consider in this work the capillaries and the tissue as two coupled porous media, i.e., a double continuum approach [17]. In addition to that we discuss alternative coupling conditions between the 1D vessels and the 3D continuum for the capillaries. To validate our *hybrid 3D-1D* modeling approach, a comparison with a *fully-discrete 3D-1D* model [8, 10, 11, 37, 30] is performed.

The rest of this work is structured as follows. In Section 2, we describe the data set that is used for our numerical tests. In addition to that the basic modeling assumptions are discussed. The model problems and the corresponding numerical discretization methods are outlined in Section 3. Section 4 contains some numerical tests and a discussion of the results obtained from both models. Finally in Section 5, we summarize the key features of our work and give a short outlook.

2 Problem setting and main simplifications

In order to illustrate the performance of our modeling approaches, we consider the microvascular network shown in Fig. 1. To obtain the data for this microvascular network, firstly an anaesthetized rat was perfused with phosphate buffered saline and barium sulphate. In a second step, the brain was removed and a sample from the cortex was taken.

Using this sample, an X-ray tomographic microscopy of the sample was performed. Based on the resulting image, vessel midlines were extracted, and the 3D coordinates of branches, kinks as well as start and end points were determined. We denote these points as network nodes. Furthermore, curved vessel midlines were replaced by straight edges and to each edge, a mean vessel radius was assigned. Besides the different radii also the connectivity of network nodes was determined, i.e., it was reported, which network nodes are connected with each other. At the network nodes that are adjacent to the boundaries of the extracted sample, physiologically meaningful pressure boundary conditions are provided [45].

Analyzing the given data, it turns out that the radii range from $1.6 \mu\text{m}$ to $28.2 \mu\text{m}$. Within the network some larger penetrating arterioles and venules can be identified at the top of the sample. At the bottom of the sample a larger venule and arteriole are leaving or entering the cuboid domain. The rest of the microvascular network consists of tiny capillaries. Zooming into the original data set, we detected some dead ends of the arterioles and venules (network nodes that are not connected to the capillaries). Since we want to perform a precise comparison between the fully discrete and the hybrid modeling approach, the edges associated with dead ends are removed from the data set such that in the

resulting microvascular network all the network nodes are connected. Further modeling assumptions that are used in the remaining sections, read as follows:

- (A1) The non-Newtonian flow behavior of blood is modeled in a simplified way using an algebraic relationship.
- (A2) The density of blood is constant.
- (A3) The influence of gravity is neglected.
- (A4) The inertial effects can be neglected.
- (A5) The pulsatility can be neglected.
- (A6) The walls of the larger vessels are considered impermeable, i.e., no flow occurs across their walls.

These assumptions are motivated by the following considerations: It is well known that blood consists beside plasma also of blood cells. Blood plasma itself is a mixture of water and ions, while the blood cells can be separated into the following groups: red blood cells, white blood cells and blood platelets [19] (Chap. 1). In particular the red blood cells determine the flow behavior of blood significantly [18]. Moving through a microvascular network the red blood cells have to deform more and more as the vessel diameters become smaller than the diameter of the red blood cells. This results in a varying viscosity for the individual blood vessels and therefore this feature is recorded in (A1) [23]. Thereby, we adopt for an edge of diameter D the following formula for the in vivo viscosity μ_{bl} [Pa · s] [42]:

$$\mu_{bl}(D) = \mu_p \left(1 + (\mu_{0.45} - 1) \frac{(1-H)^C - 1}{(1-0.45)^C - 1} \cdot \left(\frac{D}{D-1.1} \right)^2 \right) \cdot \left(\frac{D}{D-1.1} \right)^2. \quad (1)$$

Please note that in (1) the diameter D is dimensionless. The physical diameter d [μm] has to be divided by $1.0 \mu\text{m}$ to obtain D . The viscosity of the blood plasma is denoted by μ_p [Pa · s], and H stands for the discharge hematocrit which is defined by the ratio between the volume of the red blood cells and the total blood volume. The apparent viscosity $\mu_{0.45}$ for a discharge hematocrit of 0.45 is calculated by:

$$\mu_{0.45} = 6.0 \exp(-0.085 \cdot D) + 3.2 - 2.44 \exp(-0.06 \cdot D^{0.645})$$

and C is a coefficient determining the influence of H on μ_{bl} :

$$C = (0.8 + \exp(-0.075 \cdot D)) \left(-1 + \frac{1}{1 + 10^{-11} D^{12}} \right) + \frac{1}{1 + 10^{-11} D^{12}}.$$

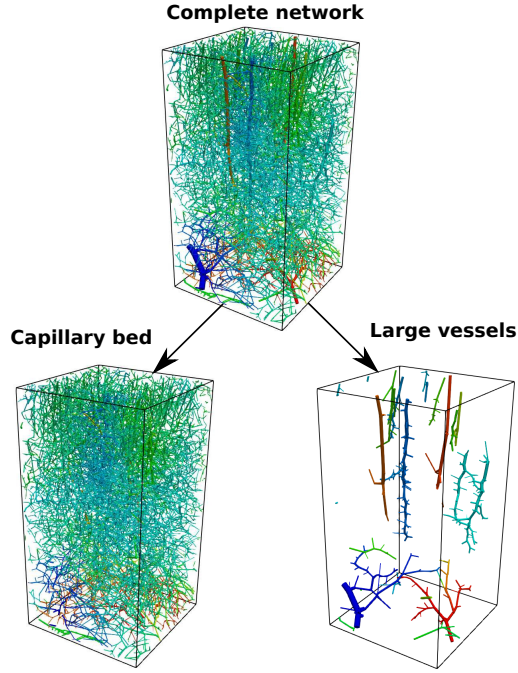


Figure 1: A microvascular network extracted from a rat brain (top), filling a volume of $1\text{ mm} \times 1\text{ mm} \times 2\text{ mm}$. A subdivision based on the vessel radius can be seen at the bottom of the figure. The network at the bottom left, is the capillary bed of the microvascular network (all vessels whose radii are smaller than a given threshold, here $7\text{ }\mu\text{m}$). The motivation for such threshold is postponed to Section 4.1. At the bottom right, arterioles and venules (whose radii are larger than the given threshold) constitute the network of larger vessels.

Please note that this function for the in vivo viscosity holds actually for human blood. However we are not aware of such a function for rat blood, and therefore we assume that this function can be employed for rat blood as well. For simplicity, we assume in (A2) that blood is incompressible. Considering the total volume of the system under consideration, the quantity of fluids contained in this volume is relatively small, such that the effect of gravity can be neglected. Since the blood velocity is about 0.1 mm/s in the arterioles and venules and about 0.01 mm/s in the capillary bed in a human system [19, Tab. 1.7], it can be concluded that the Reynolds numbers in the whole microvascular network are significantly lower than 1.0. Therefore modeling assumption (A4) is reasonable [21]. The pulsatility of blood flow can be neglected (A5), due to the fact that the Womersley numbers in the arterioles, venules and the capillaries are much smaller than 0.1. The Womersley number is a dimensionless number relating the frequency of a pulse and the viscosity of a fluid to each other [19, Tab. 1.7]. The last modeling assumption (A6) is motivated by the fact that the vessel walls of capillaries consist of a thin layer of endothelial cells with gaps between them such that blood plasma, oxygen and other substances can migrate into the interstitial space and then to the tissue cells or vice versa. Contrary

to that, the vessel walls of the larger vessels (arterioles and venules) are thicker and not as permeable, since they exhibit a continuous endothelial cell layer that is surrounded by one or two concentric layers of smooth muscle cells [12] [19, Chap.1].

3 Models and numerical methods

After describing the data set used in this work and discussing the basic modeling assumptions, we outline in this section the two modeling approaches under consideration, i.e., the fully-discrete 3D-1D model and the hybrid 3D-1D model. In particular, we discuss coupling concepts between the different parts of the microvascular network and the tissue. Finally, the numerical discretization of the model equations is shortly explained.

We start by introducing some notation. The cuboid containing the microvascular network depicted in Fig. 1 is denoted by Ω and given by:

$$\Omega = \left\{ \mathbf{x} = (x_1, x_2, x_3)^\top \mid 0 \text{ mm} < x_1, x_2 < 1.13662 \text{ mm} \right. \\ \left. \wedge 8.75 \cdot 10^{-4} \text{ mm} < x_3 < 2.16388 \text{ mm} \right\}.$$

As it has been described in Section 2, we assume that the vascular system Λ under consideration has been segmented and approximated by extracting the midline of each blood vessel and approximating the midlines by straight segments $\Lambda_k \subset \Lambda$. Each segment is equipped with a constant radius value R_k for $k = 1, \dots, N$. Therefore, the entire vascular system is assumed to be given by the union of N cylinders V_k of radius R_k for $k = 1, \dots, N$. We then split the domain in two parts:

$$\Omega_v = \bigcup_{i=1}^N V_i \quad \text{and} \quad \Omega_t = \Omega \setminus \Omega_v,$$

where Ω_v represents the vascular system and Ω_t the tissue. The entire vascular system can now be described by a graph, whose edges are represented by the center lines Λ_k of each cylinder V_k , for $k = 1, \dots, N$. Each segment Λ_k is parametrized by the arc length s_k , and λ_k is the tangent unit vector determining the orientation of the centerline of V_k . Let us denote the two endpoints of the edge Λ_k by $\mathbf{x}_{k,1}, \mathbf{x}_{k,2} \in \Omega$. With this notation at hand, each cylinder V_k can be defined as:

$$V_k = \{ \mathbf{x} \in \Omega_v \mid \mathbf{x} = \mathbf{x}_{k,1} + s_k \cdot \lambda_k + \mathbf{r}_k \},$$

where $\mathbf{x}_{k,1} + s_k \cdot \lambda_k \in \Lambda_k = \mathcal{M}_k(\Lambda' \subset \mathbb{R}^1)$ and

$$\mathbf{r}_k \in \mathcal{D}_{\Lambda_k}(R_k) = \{ r \mathbf{n}_{\Lambda_k}(s_k, \theta) : r \in [0, R_k), s_k \in (0, |\mathbf{x}_{k,2} - \mathbf{x}_{k,1}|), \theta \in [0, 2\pi) \}.$$

\mathcal{M}_k is a mapping from a reference domain Λ' to the manifold $\Lambda_k \subset \Omega$, and \mathbf{n}_{Λ_k} denotes the set of unit normal vectors with respect to Λ_k . Γ_k is the lateral surface of the branch V_k , and the union Γ corresponds approximately to the surface of the vascular system, since the cylinders V_k may not perfectly match to each other: $\Gamma = \bigcup_{k=1}^N \Gamma_k$. The given blood vessel network is separated into two parts: Based on a fixed threshold R_T , we subdivide the network Λ in two

subsets Λ_L consisting of large vessels, which are considered to be impermeable and Λ_C consisting of capillaries. Associated to this separation, we define two index sets I_L, I_C :

$$I_L := \{k \in \{1, \dots, N\} \mid R_k \geq R_T\} \quad \text{and} \quad I_C := \{k \in \{1, \dots, N\} \mid R_k < R_T\}.$$

Using these definitions, Λ_L and Λ_C can be represented as follows:

$$\Lambda_L := \bigcup_{k \in I_L} \Lambda_k \quad \text{and} \quad \Lambda_C := \bigcup_{k \in I_C} \Lambda_k.$$

The surface of the capillaries is given by: $\Gamma_C := \bigcup_{k \in I_C} \Gamma_k$. Finally, to each node of the graph a pressure value is assigned. The computation of the pressure values corresponding to the interior nodes is outlined in Section 3.3, while at the boundary nodes the pressure values are prescribed from the given data set (see Section 2).

3.1 Fully-discrete 3D-1D model

With respect to the surrounding tissue, we assume that it can be considered as a porous medium with an isotropic scalar permeability K_t [m^2] [28]. In order to model the flow in a porous medium, one can use the Darcy equation to obtain a pressure field [1, 24].

Within the 1D network Λ , we assume that the flow is described by Hagen-Poiseuille's law with a mass balance equation. Differentiation over the branches is defined using the tangent unit vector as $dw/ds_k = \nabla w \cdot \boldsymbol{\lambda}_k$ on Λ_k , i.e. d/ds_k represents the projection of ∇ along $\boldsymbol{\lambda}_k$. The governing flow equations for the whole network Λ are obtained by summing the governing equation over the index k and introducing the global variable s . Furthermore, we assume that the mass transfer from the vessel into the tissue matrix and vice versa occurs across the membrane Γ_C of the capillaries according to Starling's filtration law [32, 51]. Following the approach presented in [30], these exchanges processes are accounted for by a Dirac measure δ_{Γ_C} in the source term of the 3D tissue problem:

$$\left\{ \begin{array}{ll} -\nabla \cdot \left(\rho_{\text{int}} \frac{K_t}{\mu_{\text{int}}} \nabla p^t \right) = L_{\text{cap}} \rho_{\text{int}} \left(p^v - \bar{p}^t - (\pi_p - \pi_{\text{int}}) \right) \delta_{\Gamma_C}, & \text{in } \Omega, \\ -\frac{d}{ds} \left(\rho_{\text{bl}} \pi R^2 \frac{K_v}{\mu_{\text{bl}}} \frac{dp^v}{ds} \right) = 2\pi R L_{\text{cap}} \rho_{\text{int}} \left(\bar{p}^t - p^v + (\pi_p - \pi_{\text{int}}) \right), & \text{in } \Lambda, \\ \rho_{\text{int}} \frac{K_t}{\mu_{\text{int}}} \nabla p^t \cdot \mathbf{n} = 0, & \text{on } \partial\Omega, \\ p^v = p_D^v, & \text{on } \partial\Lambda, \end{array} \right. \quad (2)$$

For each edge Λ_k and its lateral surface Γ_k and $f \in L^2(\Gamma_k)$, we indicate with $f\delta_{\Gamma_k}$ the linear operator in $\mathcal{C}(\Omega)$ defined by

$$\langle f\delta_{\Gamma_k}, \phi \rangle = \int_{\Lambda_k} \int_{\partial B(s_k, R_k)} f\phi \, dS \, ds_k, \quad \forall \phi \in \mathcal{C}_0^\infty(\Omega), \quad k \in I_C.$$

The symbol $\partial B(s_k, R_k)$ denotes the circle with center in $\Lambda_k(s_k)$ and perpendicular to $\mathbf{\lambda}_k$. The variable p^v denotes the pressure in the network and p^t the pressure in the tissue. The term $\overline{p^t}(s_k)$ in (2) represents the average value of p^t with respect to the circle $\partial B(s_k, R_k)$:

$$\overline{p^t}(s_k) = \frac{1}{2\pi R_k} \int_0^{2\pi} p^t(\Lambda_k(s_k) + R_k \mathbf{n}_{\Lambda_k}(s_k, \theta)) R_k d\theta, \quad k \in I_C. \quad (3)$$

π_p and π_{int} represent the oncotic pressures of the plasma and the interstitial fluid, respectively. According to [33], these values are assumed to be constant. The hydraulic conductivity L_{cap} [m/(Pa · s)] of the membrane is assumed to be constant for the segments Λ_k , $k \in I_C$. The radius R [m] and the permeability K_v [m²] are defined for each segment Λ_k as:

$$R|_{\Lambda_k} = R_k \text{ and } K_v|_{\Lambda_k} = \frac{R_k^2}{8}. \quad (4)$$

The viscosity μ_{bl} [Pa · s] of blood is computed according to (1), while μ_{int} [Pa · s] represents the viscosity of interstitial fluid. ρ_{int} [kg/m³] and ρ_{bl} [kg/m³] are the densities of the interstitial fluid and of blood, respectively. p_D^v [Pa] are the boundary data, obtained from the data set previously described in Section 2. On the boundary of the tissue continuum $\partial\Omega \subseteq \partial\Omega_t \setminus \Gamma_C$, we set homogeneous Neumann boundary conditions. Due to the fact that we have no boundary data available homogeneous Neumann boundary conditions have been chosen. However, if measurements or other data become available, this boundary condition can easily be replaced.

Alternative 3D-1D PDE-systems simulating flow in microvascular networks, can be found in [10, 11]. The difference to the presented coupling approach is that in the source term of the tissue problem, the Dirac measure is concentrated on the midlines of the vascular system. As a result singularities along the network midlines are introduced in the 3D pressure field [31, 22]. Moreover, there are no estimates for the modeling errors arising from this type of coupling concepts. In [30] we proved for a two-dimensional model problem that the coupling approach in (2) causes a small modeling error, if the radii of the network are small compared to the considered tissue matrix. Furthermore, the pressure field in the 3D tissue matrix does not exhibit any singularities, but only kinks at vessel surfaces.

3.2 Hybrid 3D-1D model

Considering the microvascular network in Fig. 1, it can be seen that it consists of venules and arterioles and a large number of small capillary vessels forming a dense structure. Due to that, we consider the capillaries as a 3D porous medium, while the venules and arterioles are still considered as 1D vessel systems. This approach has the clear advantage that it does not require a high-resolution description of the microvascular network under consideration and that it preserves the hierarchy of the larger vessels. All in all, there are now two coupled 3D continua in Ω , one for the capillary bed and another one for the tissue. This means that the hybrid 3D-1D model is a *double-3D continuum* model contrary to the *fully-discrete* model, which is a *single-3D continuum* model. As for the tissue,

the flow in the homogenized capillaries can be described using Darcy's law, and we pose the following problem for the corresponding unknown p^{cap} :

$$\begin{cases} -\nabla \cdot \left(\rho_{\text{bl}} \frac{K_{\text{up}}}{\mu_{\text{bl}}^{\text{up}}} \nabla p^{\text{cap}} \right) = q^{\text{cap}}, & \text{in } \Omega, \\ p^{\text{cap}} = p_{\text{D}}^{\text{cap}}, & \text{on } \partial\Omega. \end{cases} \quad (5)$$

K_{up} is the corresponding permeability tensor, $\mu_{\text{bl}}^{\text{up}}$ is an averaged viscosity, q^{cap} indicates the source term and $p_{\text{D}}^{\text{cap}}$ denotes the Dirichlet boundary condition. These terms and parameters are described in the following.

Computing the tensor K_{up} and the averaged viscosity $\mu_{\text{bl}}^{\text{up}}$

Let us assume that the domain Ω can be decomposed into *representative elementary volumes* (REV_s) [24], that is:

$$\overline{\Omega} = \bigcup_{j=1}^{N_{\text{REV}}} \overline{\text{REV}_j}, \quad (6)$$

where N_{REV} is the total number of REV_s. Furthermore, we assume that each $\text{REV}_j \subset \Omega$ is a rectangular cuboid, as depicted in Fig. 2. With respect to REV_j , the viscosity $\mu_{\text{bl}}^{\text{up}}$ is defined as follows:

$$\mu_{\text{bl}}^{\text{up}}(\mathbf{x}) = \mu_{\text{bl},j}^{\text{up}}, \text{ if } \mathbf{x} \in \text{REV}_j, \text{ where } \mu_{\text{bl},j}^{\text{up}} = \frac{1}{|I_{C,j}|} \sum_{k \in I_{C,j}} \mu_{\text{bl}}(2 \cdot R_k / \mu m).$$

The viscosity μ_{bl} is given by (1), and the set $I_{C,j}$ is defined as follows:

$$I_{C,j} = \{k \in I_C \mid \Lambda_k \cap \text{REV}_j \neq \emptyset\}.$$

Now, we determine the tensor K_{up} which represents the permeability of the homogenized capillary bed. In [15], the authors computed full permeability tensors for periodic cells based on computer-generated capillary networks, whose properties statistically match measurements in brain tissue. The off-diagonal entries were found to be on average two orders of magnitude smaller than the diagonal terms [15, Table 2]. Following this observation, we make the following simplifying assumptions for K_{up} :

- (i) the permeability tensor K_{up} is constant on each REV_j :

$$K_{\text{up}}(\mathbf{x}) = K_{\text{up}}^{(j)}, \text{ if } \mathbf{x} \in \text{REV}_j.$$

- (ii) the permeability tensor $K_{\text{up}}^{(j)}$ is diagonal:

$$K_{\text{up}}^{(j)} = \begin{pmatrix} k_x^{(j)} & 0 & 0 \\ 0 & k_y^{(j)} & 0 \\ 0 & 0 & k_z^{(j)} \end{pmatrix},$$

with $k_x^{(j)}, k_y^{(j)}, k_z^{(j)} > 0$.

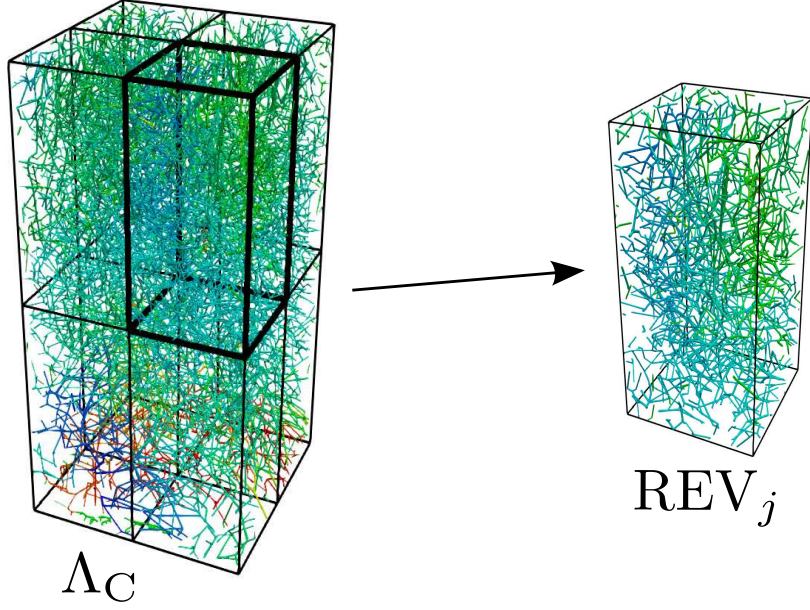


Figure 2: Subdivision of the capillaries Λ_C into eight REV_s.

In order to determine the components of the permeability tensor $K_{\text{up}}^{(j)}$, we apply the upscaling strategy presented in [45] which we briefly describe in the following. For simplicity, we restrict ourselves to the computation of the permeability component $k_x^{(j)}$. The other permeability components $k_y^{(j)}$ and $k_z^{(j)}$ can be computed in an analogous way. As a first step to compute this quantity, we apply a no-flow boundary condition to all the facets of the REV_j whose face normals are not aligned with the x -axis (see Fig. 3). The remaining facets are denoted by $F_{\text{in},x}^{(j)}$ and $F_{\text{out},x}^{(j)}$. Between these facets a pressure gradient is applied by imposing a pressure $p_{\text{in},x}$ on $F_{\text{in},x}^{(j)}$ and a pressure $p_{\text{out},x}$ on $F_{\text{out},x}^{(j)}$, where $p_{\text{in},x} > p_{\text{out},x}$. This results into a volume flux from $F_{\text{in},x}^{(j)}$ to $F_{\text{out},x}^{(j)}$. Using the Vascular Graph Model (VGM) described in Subsection 3.3, we compute the pressure field in

$$\Lambda_{C,j} = \bigcup_{k \in I_{C,j}} \Lambda_k.$$

By means of this pressure field, the volume flux $VF_{\text{out},x}^{(j)}$ through $F_{\text{out},x}^{(j)}$ is computed as follows:

$$VF_{\text{out},x}^{(j)} = \sum_{\mathbf{x}_k \in \Lambda_{C,j} \cap F_{\text{out},x}^{(j)}} \frac{\pi R_k^2 K_v(s_k)}{\mu_{\text{bl}}} \cdot \frac{\partial p^v}{\partial s}(s_k),$$

where $\mathbf{x}_k = \Lambda_k(s_k)$ for $k \in I_{C,j}$. Based on $VF_{\text{out},x}^{(j)}$, the permeability component $k_x^{(j)}$ is approximated as follows:

$$k_x^{(j)} \approx \frac{VF_{\text{out},x}^{(j)} \cdot \mu_{\text{bl},j}^{\text{up}} \cdot L_x^{(j)}}{L_y^{(j)} \cdot L_z^{(j)} \cdot (p_{\text{in},x} - p_{\text{out},x})}. \quad (7)$$

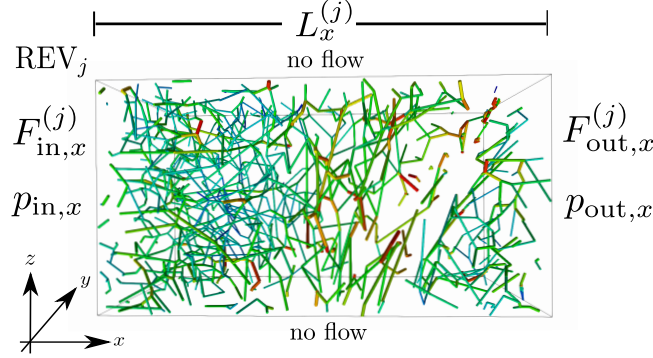


Figure 3: Homogenization of a capillary network contained in a REV_j . On the facets $F_{\text{in},x}^{(j)}$ and $F_{\text{out},x}^{(j)}$ whose normals are aligned with the x -axis, we apply pressures $p_{\text{in},x}$ and $p_{\text{out},x}$, while on the other facets a no-flow condition is imposed. Computing the flux between $F_{\text{in},x}^{(j)}$ and $F_{\text{out},x}^{(j)}$, the permeability component $k_x^{(j)}$ can be estimated.

$L_x^{(j)}$, $L_y^{(j)}$ and $L_z^{(j)}$ are the edge lengths of REV_j in the x -, y - and z -direction, respectively. An open issue in this context is the choice of the REV-size. In order to clarify this issue, we refer to Subsection 4.2, in which the admissible size of the REVs is determined numerically.

Computing the boundary conditions p_D^{cap}

For the computation of the boundary data p_D^{cap} , we consider the REV_j that are adjacent to the boundary $\partial\Omega$, i.e., $\overline{\text{REV}_j} \cap \partial\Omega \neq \emptyset$. The six facets of a REV_j are denoted by F_{1j}, \dots, F_{6j} . For each F_{ij} with $F_{ij} \subset \partial\Omega$, we compute an averaged boundary value $p_D^{(ij)}$. This is done, by averaging all the pressure values p_k that are assigned to the boundary nodes $\mathbf{x}_k \in \partial\Lambda_C$ and whose distance to the face F_{ij} is smaller than a small parameter $\varepsilon_d > 0$ (see Fig. 4): $\text{dist}(F_{ij}, \mathbf{x}_k) < \varepsilon_d$. For the rest of the paper, we set $\varepsilon_d = 10^{-8}$ m. Assuming that N_{ij} nodes are fulfilling these conditions, we compute the averaged pressure by an arithmetic mean:

$$p_D^{(ij)} = \frac{1}{N_{ij}} \sum_{k=1}^{N_{ij}} p_k.$$

In order to obtain a smooth function for the boundary values p_D^{cap} , we assign the pressure values $p_D^{(ij)}$ to the centers of the faces F_{ij} and construct a linear interpolant p_D^{cap} on $\partial\Omega$ based on the described setup by means of the function `interpolate` from the package PDELab of Dune [5].

Computing the source term q^{cap}

The source term q^{cap} in (5) can be splitted into a component q_v^{cap} accounting for the impact of the larger vessels and a component q_t^{cap} incorporating the influence of the surrounding tissue:

$$q^{\text{cap}} = q_v^{\text{cap}} + q_t^{\text{cap}}. \quad (8)$$

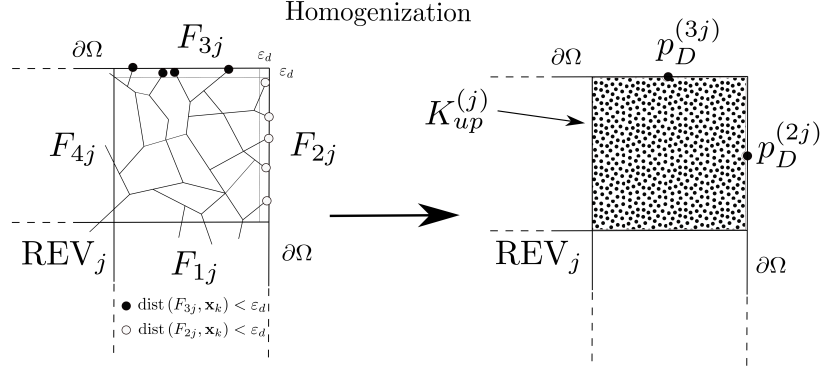


Figure 4: The figure shows a two dimensional layout parallel to the x - y plane of an REV_j that is located at an edge of the domain Ω . At the top of the figure, the discrete capillary network contained in REV_j is shown, while in the bottom part of the figure, the homogenized system with the tensor $K_{\text{up}}^{(j)}$ and the averaged boundary pressures $p_D^{(2j)}$ and $p_D^{(3j)}$ can be seen.

Let \mathbf{x}_k be a node at the boundary of the subset Λ_L and in the interior of the domain Ω , i.e., $\mathbf{x}_k \in \partial\Lambda_L \cap \Omega$. Furthermore, we assume that $\mathbf{x}_k \in \Lambda_k \cap \text{REV}_j$ for an index $k \in I_L$ and an index $j \in \{1, \dots, N_{\text{REV}}\}$. This means, there exists a s_k such that $\mathbf{x}_k = \Lambda_k(s_k)$. Then the flux occurring between the edge Λ_k and the capillary continuum is given by:

$$\rho_{\text{bl}} \frac{\pi R_k^2 K_v(s_k)}{\mu_{\text{bl}}} \cdot \frac{\partial p^v}{\partial s}(s_k) = \alpha_v^{\text{cap}}(\Lambda_k, \text{REV}_j) \left(p_{(j)}^{\text{cap}} - p^v(s_k) \right), \quad (9)$$

where the factor α_v^{cap} and the averaged pressure $p_{(j)}^{\text{cap}}$ are defined as follows:

$$\alpha_v^{\text{cap}}(\Lambda_k, \text{REV}_j) = \rho_{\text{bl}} \cdot \frac{\pi R_k^2 K_v^{(j)}}{\mu_{\text{bl}} \ell_c^{(kj)}} \quad \text{and} \quad p_{(j)}^{\text{cap}} = \frac{1}{|\text{REV}_j|} \int_{\text{REV}_j} p^{\text{cap}}(x) \, dx. \quad (10)$$

The coefficient $K_v^{(j)}$ represents the permeability of the capillaries connected to the coupling point \mathbf{x}_k . The parameter $\ell_c^{(kj)}$ [m] indicates the average length of the blood flow paths that begin at \mathbf{x}_k and are contained in REV_j which is not known a priori and has to be estimated. Therefore, we set:

$$\frac{K_v^{(j)}}{\ell_c^{(kj)}} = \alpha \frac{\overline{K_v^{(j)}}}{L_j}, \quad (11)$$

where L_j is the smallest edge length of the REV_j , and $\overline{K_v^{(j)}}$ denotes the arithmetic average of the permeabilities (4) of the capillaries contained in the REV_j . A numerical study to determine the optimal value of the parameter $\alpha \in (0, 1)$ (with respect to the fluxes within the system) for the problem under consideration is postponed to Subsection 4.3. Considering the right hand side of (9) one has to note that the term

$$\frac{p_{(j)}^{\text{cap}} - p^v(s_k)}{\ell_c^{(kj)}}$$

represents a finite difference approximation of a pressure gradient at an outlet of the larger vessels. According to the REV-concept in porous media theory [1, 24], one can assign to each REV an averaged pressure $p_{(j)}^{\text{cap}}$, which stands for the pressure field in the REV_j . The finite difference above can be considered as an approximation of the pressure gradient between an outlet of Λ_L and the homogenized capillary bed in REV_j . Using (9), the source term q_v^{cap} is computed for $\mathbf{x} \in \text{REV}_j$ by:

$$q_v^{\text{cap}}(\mathbf{x}) = \sum_{\mathbf{x}_k \in \partial\Lambda_L \cap \text{REV}_j} \frac{\alpha_v^{\text{cap}}(\Lambda_k, \text{REV}_j)}{|\text{REV}_j|} \left(p^v(s_k) - p_{(j)}^{\text{cap}} \right), \quad (12)$$

such that the model is mass conservative.

Computing the source term q_t^{cap}

As in the case of the fully-discrete 3D-1D model, the tissue is considered as a porous structure. The main difference to the capillaries is that we assume an isotropic permeability K_t for the tissue. Furthermore the interstitial fluid is assumed to have a constant viscosity μ_{int} . By means of Darcy's law, the pressure p^t can be computed by:

$$\begin{cases} -\nabla \cdot \left(\rho_{\text{int}} \frac{K_t}{\mu_{\text{int}}} \nabla p^t \right) = -q_t^{\text{cap}}, & \text{in } \Omega, \\ \rho_{\text{int}} \frac{K_t}{\mu_{\text{int}}} \nabla p^t \cdot \mathbf{n} = 0, & \text{on } \partial\Omega. \end{cases} \quad (13)$$

It remains to specify the source term q_t^{cap} modeling the fluid transfer between the capillary bed and the intracellular space. For this purpose, we use as in (2) Starling's filtration law with respect to the vessel surface area S_j that is contained in an REV_j :

$$S_j = \sum_{k \in I_{C,j}} \left| \tilde{\Lambda}_k \right| \cdot 2\pi R_k,$$

where $\tilde{\Lambda}_k \subseteq \Lambda_k$ such that $\Lambda_k \cap \text{REV}_j = \tilde{\Lambda}_k$. Using this parameter, q_t^{cap} is given by:

$$q_t^{\text{cap}}(\mathbf{x}) = \frac{\rho_{\text{int}} \cdot S_j \cdot L_{\text{cap}}}{|\text{REV}_j|} \left(p^t(\mathbf{x}) - p^{\text{cap}}(\mathbf{x}) + (\pi_p - \pi_{\text{int}}) \right), \quad \mathbf{x} \in \text{REV}_j. \quad (14)$$

Summary of the equations governing the hybrid model

Summarizing all the previous considerations, the hybrid (double-continuum) 3D-3D-1D model is governed by the following equations:

- Large Vessels (1D discrete network):

$$\begin{cases} -\frac{\partial}{\partial s} \left(\rho_{\text{bl}} \cdot \pi R^2 \frac{K_v}{\mu_{\text{bl}}} \frac{\partial p^v}{\partial s} \right) = 0, & \text{in } \Lambda_L, \\ p^v = p_D^v, & \text{on } \partial\Lambda_L \cap \partial\Omega, \\ \text{flux term in (9),} & \text{on } \partial\Lambda_L \cap \Omega. \end{cases} \quad (15)$$

- Capillary bed (3D porous medium):

$$\begin{cases} -\nabla \cdot \left(\rho_{\text{bl}} \frac{K_{\text{up}}}{\mu_{\text{bl}}} \nabla p^{\text{cap}} \right) = q_v^{\text{cap}} + q_t^{\text{cap}}, & \text{in } \Omega, \\ p^{\text{cap}} = p_D^{\text{cap}}, & \text{on } \partial\Omega. \end{cases} \quad (16)$$

- Tissue (3D porous medium):

$$\begin{cases} -\nabla \cdot \left(\rho_{\text{int}} \frac{K_t}{\mu_{\text{int}}} \nabla p^t \right) = -q_t^{\text{cap}}, & \text{in } \Omega, \\ \rho_{\text{int}} \frac{K_t}{\mu_{\text{int}}} \nabla p^t \cdot \mathbf{n} = 0, & \text{on } \partial\Omega. \end{cases} \quad (17)$$

The coupling term q_v^{cap} is given by (12), and describes the interactions between the extracted network Λ_L and the homogenized capillaries. The other coupling term q_t^{cap} is defined by (14), and stands for the exchange between tissue and homogenized capillaries.

3.3 Numerical discretizations

Next, we briefly describe a numerical scheme that is used to solve the model equations (2) and (15)-(17). The elliptic PDEs governing the flow within the tissue or the upscaled capillaries are solved numerically by means of a standard cell-centered finite volume method [24], where the numerical fluxes across the cell surfaces are approximated by the two-point flux method. The choice of this method is motivated by its intrinsic local mass conservation, and by the fact that we can work with uniform hexahedral meshes.

For the numerical solutions of the network equations in both modeling approaches (2) and (15), we employ the vascular graph model (VGM) [17, 40, 45]. Thereby, we approximate the pressure values at the grid nodes \mathbf{x}_k discretizing the network structures. Around each grid node a control volume CV_k is placed such that the grid node is in the center of the control volume (see Fig. 5). In the next step, the fluxes F_{kj} and F_k^t across the surfaces of the control volume are computed and summed up such that the sum of the fluxes is equal to zero:

$$\sum_{j \in \mathcal{N}(\mathbf{x}_k)} F_{kj} - F_k^t = 0, \quad F_{kj} = \frac{\rho_{\text{bl}} \cdot \pi R_k^4}{8\mu_{\text{bl}} |\mathbf{x}_j - \mathbf{x}_k|} \cdot \left(p^v(\mathbf{x}_j) - p^v(\mathbf{x}_k) \right), \quad (18)$$

where R_k is the radius of the edge linking \mathbf{x}_k and \mathbf{x}_j . $\mathcal{N}(\mathbf{x}_k)$ denotes the set of indices that share the edge Λ_k with the point \mathbf{x}_k .

Solving the fully discrete model (2), the walls of the smaller vessels (capillaries) are permeable, and a flux across the vessel walls has to be considered, too. This is done by computing an averaged pressure in the tissue with respect to the part of the vessel wall touching the control volume, see Fig. 5. Then, this pressure value is compared to the network pressure associated with the grid node \mathbf{x}_k to determine the flux across the vessel wall:

$$F_k^t = 2\pi L_{\text{cap}} \cdot \rho_{\text{int}} \left[\sum_{j \in \mathcal{E}(\mathbf{x}_k)} R_j \int_{\text{CV}_k \cap \Lambda_j} I(p^v) - \bar{p}^t - (\pi_p - \pi_{\text{int}}) dS \right].$$

$\mathcal{E}(\mathbf{x}_k)$ is the index set for the edges containing the grid node \mathbf{x}_k . $I(p^v)$ is a linear interpolant for the pressure field p^v , whose shape on each edge is determined by the two pressure values of the edge. By this, we obtain for each grid node a mass balance equation. Summarizing these equations, we obtain a system of equations for the pressure values at the grid nodes.

The reason why we consider a different discretization for the network is the treatment of bifurcations or junctions in the network. Within the VGM approach, a grid node is placed directly at a bifurcation and the mass balance equation (18) can easily be established. Applying the cell-centered finite volume method, one cannot place a degree of freedom directly at a bifurcation, and therefore the fluxes through the bifurcation point have to be computed. Since the radii of the branches and the main vessel may be different, the computation of the fluxes requires a careful computation of the numerical transmissibility coefficients in (18). Finally, the continuity of the pressure at a bifurcation is guaranteed using the VGM.

All in all the numerical treatment of the PDEs together with the boundary conditions, source terms and coupling conditions, yields for each model a sparse linear system of equations. Each block of the system matrix is the discrete representative of an elliptic differential operator or a coupling term, whereas the contributions of the oncotic pressures and the boundary conditions are incorporated into the right hand side of the system of equations. For the numerical solution of the linear equation system a block AMG-preconditioner is applied. The preconditioned system is then solved by a stabilized bi-conjugate gradient method. This solver was realized using the generic interface of the ISTL-library of DUNE and its AMG implementation [3, 4].

4 Numerical tests

In this section, we test the numerical models presented in Section 3 using the data set described in Section 2. Thereby, by means of the fully-discrete 3D-1D model (2) a reference solution is computed for the hybrid model (15)-(17). The results obtained by both approaches are compared with respect to mass fluxes and averaged REV-pressures. The flow is driven by the boundary conditions, as described in Sections 3.1. and 3.2. In particular, no-flow boundary condi-

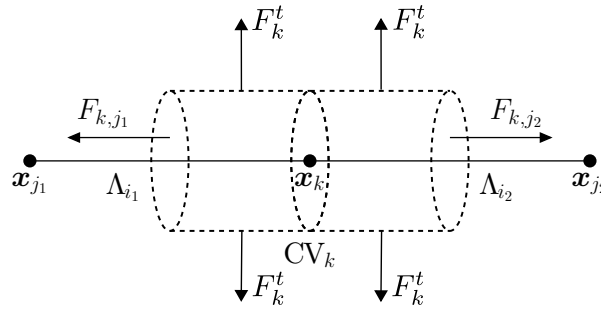


Figure 5: Representation of the numerical fluxes through the surface of the control volume CV_k with center in \mathbf{x}_k . The point shares the edges Λ_{i_1} and Λ_{i_2} with the nodes \mathbf{x}_{j_1} and \mathbf{x}_{j_2} of the network, respectively.

tions are posed for the flow in the tissue, while prescribed Dirichlet values are considered for the network (see Section 2). In Table 1, the model parameters for the numerical simulations are summarized. The motivation for the choice of $R_T = 7 \mu\text{m}$ is given in Subsection 4.1, while the number N_{REV} in (6) for the hybrid model is discussed in Subsection 4.2. Subsections 4.3 and 4.4 contain the numerical results for the mass fluxes and the averaged REV-pressures, respectively. Finally, in Subsection 4.5, the influence of different boundary conditions are discussed.

Table 1: Values of the parameters used for the numerical experiments.

Discharge hematocrit	H	0.45
Tissue permeability	K_t	10^{-18} m^2
Interstitial fluid viscosity	μ_{int}	$1.3 \cdot 10^{-3} \text{ Pa} \cdot \text{s}$
Plasma viscosity	μ_p	$1.0 \cdot 10^{-3} \text{ Pa} \cdot \text{s}$
Blood density	ρ_{bl}	1030 kg/m^3
Interstitial fluid density	ρ_{int}	1000 kg/m^3
Plasma oncotic pressure	π_p	3300 Pa
Interstitial oncotic pressure	π_{int}	666 Pa
Capillary wall hydraulic conductivity	L_{cap}	$10^{-12} \text{ m}/(\text{Pa} \cdot \text{s})$
Threshold large vessels/capillaries	R_T	$7 \mu\text{m}$

4.1 Justification of the threshold R_T

In this subsection, we motivate the choice of the threshold $R_T = 7 \mu\text{m}$ that we employ to separate the larger vessels from the capillaries. Let us consider the whole vessel system Λ as depicted in Fig. 1, on the top. For each segment Λ_k , we calculate the blood velocity v_k , where we set a constant pressure gradient of δp at the vertices:

$$v_k = \frac{R_k^2}{8.0\mu_{\text{bl},k}} \cdot \frac{\delta p}{|\Lambda_k|},$$

where $\mu_{\text{bl},k}$ is the viscosity of the blood according to (1). The distribution of the velocities is reported in Fig. 6, on the left, for the case: $\delta p = 1.0 \text{ Pa}$. Choosing the threshold R_T to $7.0 \mu\text{m}$, we obtain that the average velocity in the set Λ_C is approximately 60 times smaller than the average velocity in the set Λ_L . Furthermore, the set Λ_C consists of 14918 vessels, while only 337 vessels are contained in the set Λ_L . Despite the low number of larger vessel, the chosen threshold still allows us to capture the main geometry of the vessel system, as depicted in Fig. 6, on the right. In fact, choosing a larger threshold such as $R_T = 18.0 \mu\text{m}$ would reduce drastically the number of larger vessels, yielding a network that provides only restricted informations about the geometry of the original system. On the other hand, choosing a smaller threshold would incorporate too many vessels in the size of capillaries. Considering the morphological values listed in [16, Table 1], we can observe that the choice of our threshold is close to the lower bound of the diameter range for the arterioles. Motivated by these considerations, we fixed the threshold to $7.0 \mu\text{m}$.

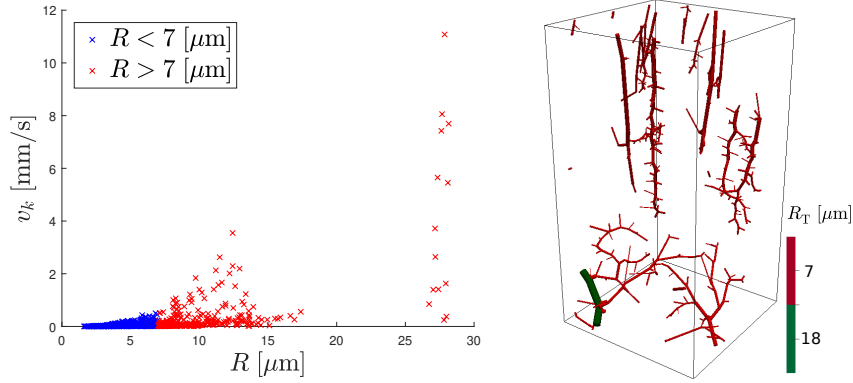


Figure 6: On the left, the blood velocity for each vessel in the system Λ is shown, where each segment is subject to a 1.0 Pa pressure difference. Setting the threshold to $R_T = 7.0 \mu\text{m}$ yields 14918 vessels in the set Λ_C with average velocity of 0.00714 mm/s, and 337 vessels in the set Λ_L with an average velocity of 0.41533 mm/s. On the right, the system Λ_L is depicted for the threshold $R_T = 7.0 \mu\text{m}$. The network Λ_L for the threshold $R_T = 18.0 \mu\text{m}$ is marked in green.

4.2 Homogenization of the capillary bed

In order to determine the admissible REV sizes for the approximation of the permeability tensor, we perform the following test: A single control volume, initially of size $12 \times 12 \times 24 \mu\text{m}$, is positioned in the center $(0.00056831, 0.00056831, 0.00113662)$ of the domain Ω and then enlarged in each space direction approximately by $4.0 \mu\text{m}$ in the x - and y -directions and by $8.0 \mu\text{m}$ in the z -direction. For each one of these control volumes, the values of the intrinsic permeability are determined using (7) and suitable adaptations for the y - and z -directions. In addition to that, we compute the *blood volume fraction*, which is defined as the ratio between the volume of the capillary network contained in the control volume under consideration and the volume of the control volume itself. The test is performed starting from the center of Ω , because this position allows for a larger margin of growth of the control volume. The numerical results confirm the expected oscillating behavior of the intrinsic permeability that typically occurs when the size of the control volume is too small (Fig. 7, left). The permeabilities appear to reach stable values, if the edges of the control volume are greater than approximately $500.0 \mu\text{m}$ (in the x - and y -direction). Therefore, we can assert that the control volume with half the dimensions of the domain $(568.31 \times 568.31 \times 1081.503 \mu\text{m})$ and collocated in the center of Ω can be assumed to be an REV. A further argument to support this statement can be derived considering the blood volume fraction of the capillary continuum. As depicted in Fig. 7 on the right, the blood volume fraction seems to stabilize around the value 1.16%, if the length of the control volume is larger than approximately $400.0 \mu\text{m}$. However, collocating a single REV in the center of the domain with half the sizes of Ω is not enough, since the entire capillary network has to be homogenized. On the other hand, having a single REV covering the entire domain would mean that the heterogeneity of the capillary system is not

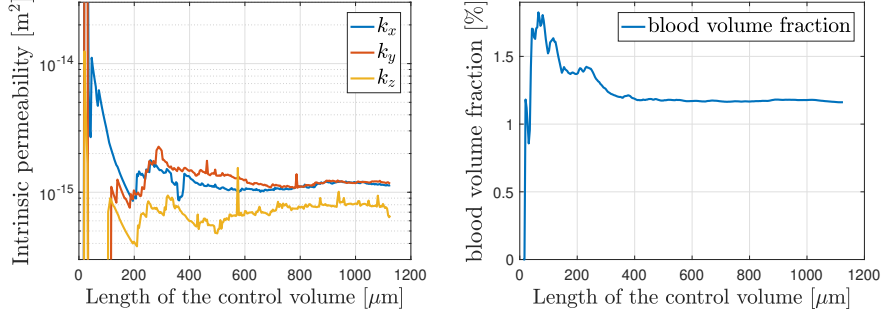


Figure 7: On the left, the upscaled permeability is computed in the case where a single control volume is positioned in the center of the domain Ω . The dimensions of the control volume are enlarged by approximately $4 \times 4 \times 8 \mu\text{m}$ in each step until the control volume fills the entire domain Ω . The length of the control volume in the plot has to be doubled to obtain the actual size of the control volume in the z -direction. After an oscillating transition zone, each permeability stabilizes around a fixed value. On the right, the blood volume fraction of the corresponding control volume is reported.

considered. In fact, observing Fig. 9 (top left), we can notice that in the upper part of the system, the capillaries are mainly aligned with the z -direction, while in the bottom part, the main directions are the x - and y -directions. These orientations are consistent with the structure of the larger vessels, as reported in Fig. 1, on the bottom right. To this end, we subdivide the domain into $2 \times 2 \times 2$ control volumes, each having half the sizes of the domain, as the central REV from the previous test. The centers of these control volumes and their corresponding numeration are reported in Table 3. To assert that these 8 control volumes are REV as well, we observe in Fig. 8 that the radii distribution of the capillaries contained in each control volume is similar to that of the central REV from the previous test. Furthermore, mean radii and standard deviations are similar as well. Supported by these observations, we can assume that the 8 control volumes considered are REV and that the permeabilities reported in Fig. 9 are representative.

4.3 Comparison of the mass fluxes

A comparison between the two numerical models is provided in terms of the mass fluxes across different boundaries and interfaces. For the one-dimensional systems in both the fully discrete network and the reduced network, the mass flux MF through a boundary node $\mathbf{x}_k = \Lambda_k(s_k) \in \partial\Lambda \cap \partial\Omega$ is computed as in (18). The inflow MF_{in} through the boundary point \mathbf{x}_k is defined as:

$$MF_{\text{in}}(\mathbf{x}_k) = \begin{cases} MF(\mathbf{x}_k), & \text{if } MF(\mathbf{x}_k) > 0, \\ 0, & \text{otherwise.} \end{cases}$$

In a similar way, we can define the mass flux out of the domain:

$$MF_{\text{out}}(\mathbf{x}_k) = \begin{cases} |MF(\mathbf{x}_k)|, & \text{if } MF(\mathbf{x}_k) < 0, \\ 0, & \text{otherwise.} \end{cases}$$

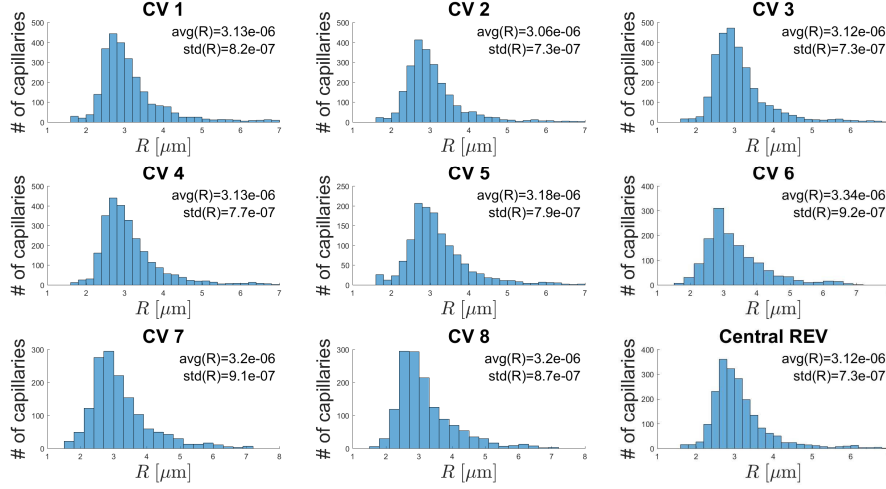


Figure 8: Histograms of the radii distributions of the capillaries contained in each control volume. The numeration is given according to Table 3. For each CV, the mean value $\text{avg}(R)$ of the radii and the standard deviation $\text{std}(R)$ are provided. In the last histogram, the radii distribution of the capillaries contained in the REV with the same center as the domain Ω and same dimensions as the other control volumes is reported.

Having this notation at hand, we define the total inflow $MF_{LV,in}$ and outflow $MF_{LV,out}$ through the large vessels as:

$$MF_{LV,in} = \sum_{\mathbf{x}_k \in \partial\Lambda_L \cap \partial\Omega} MF_{in}(\mathbf{x}_k) \quad \text{and} \quad MF_{LV,out} = \sum_{\mathbf{x}_k \in \partial\Lambda_L \cap \partial\Omega} MF_{out}(\mathbf{x}_k).$$

For the hybrid approach, the mass fluxes through the boundary $\partial\Omega$ of the capillary continuum have to be interpreted as single quantities for each boundary REV. Let us assume that the REV_j shares at least one side with the boundary of the domain, that is $\partial REV_j \cap \partial\Omega \neq \emptyset$. In this work, we employ the following definition for the *net flux* NF with respect to the REV_j :

$$NF(REV_j) = \rho_{bl} \int_{\partial REV_j \cap \partial\Omega} \frac{K_{up}^{(j)}}{\mu_{bl,j}} \cdot \nabla p_{(j)}^{cap} \cdot \mathbf{n} \, dS,$$

where \mathbf{n} denotes the outward unit normal vector to the boundary. Numerically, the gradient $\nabla p_{(j)}^{cap}$ is calculated by the standard two-point flux approximation for a cell-centered finite volume method. Analogously as for the one-dimensional fluxes, we define the inflow NF_{in} through the REV_j as:

$$NF_{in}(REV_j) = \begin{cases} NF(REV_j), & \text{if } NF(REV_j) > 0, \\ 0, & \text{otherwise,} \end{cases} \quad (19)$$

and the outflow as:

$$NF_{out}(REV_j) = \begin{cases} |NF(REV_j)|, & \text{if } NF(REV_j) < 0, \\ 0, & \text{otherwise.} \end{cases} \quad (20)$$

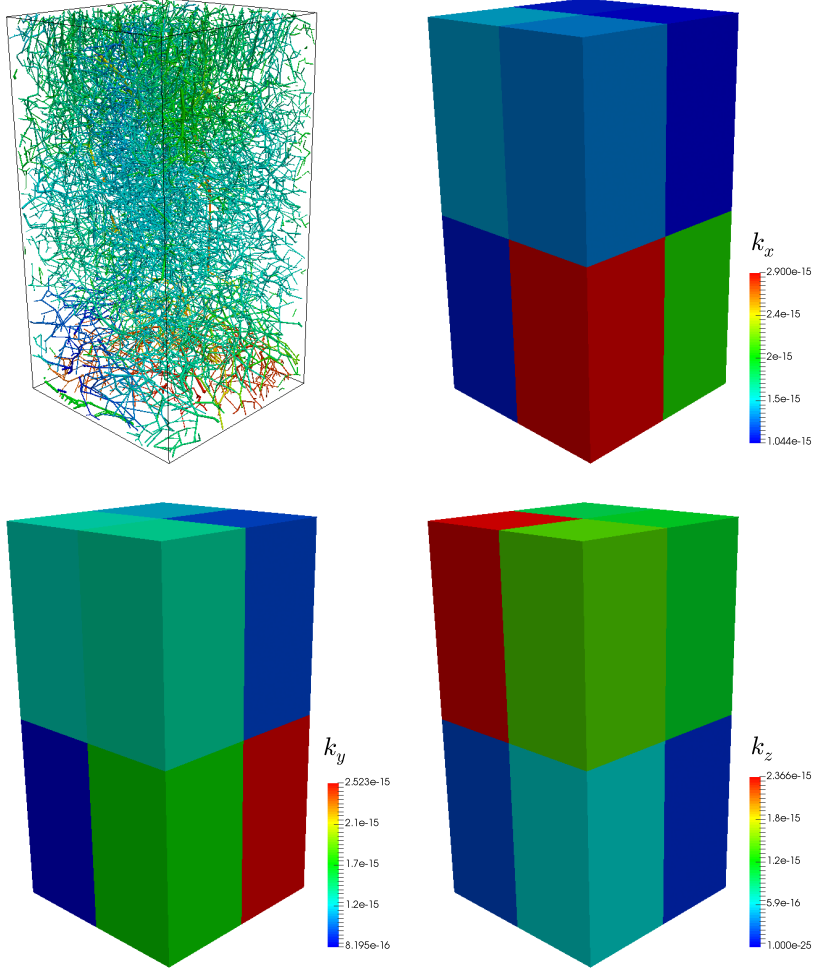


Figure 9: Permeability tensors K_{up} in the case of $2 \times 2 \times 2$ REV. The heterogeneous distribution of the capillaries from Fig. 1 is therefore incorporated, in the sense that in the lower part of the domain, the flow occurs mainly in the xy -plane, while on the top in the z -direction.

Therefore, the total net fluxes for the capillary continuum are given by:

$$MF_{\text{cap},\text{in}}^{\text{HY}} = \sum_{j=1}^{N_{\text{REV}}} NF_{\text{in}}(\text{REV}_j) \quad \text{and} \quad MF_{\text{cap},\text{out}}^{\text{HY}} = \sum_{j=1}^{N_{\text{REV}}} NF_{\text{out}}(\text{REV}_j). \quad (21)$$

For a suitable comparison of the fluxes, the fluxes through the capillaries in the fully-discrete method have to be averaged in the same sense as for the hybrid approach. Therefore, we can similarly define the net flux NF_{cap} for the REV_j as the sum of the fluxes through the boundary capillaries, namely:

$$NF_{\text{cap}}(\text{REV}_j) = \sum_{\mathbf{x}_k \in \partial\Lambda_{\text{C}} \cap \partial\text{REV}_j \cap \partial\Omega} MF(\mathbf{x}_k).$$

Then, the inflow $NF_{\text{cap},\text{in}}$ and outflow $NF_{\text{cap},\text{out}}$ through the REV_j can be defined analogously to (19) and (20). The total inflow $MF_{\text{cap},\text{in}}^{\text{FD}}$ and outflow $MF_{\text{cap},\text{out}}^{\text{FD}}$ through the capillaries for the fully-discrete model can be defined similarly to (21). The mass fluxes between capillaries and tissue are denoted by $MF_{\text{cap},\text{t}}^{\text{FD}}$ for the fully-discrete model and by $MF_{\text{cap},\text{t}}^{\text{HY}}$ for the hybrid model. Again, we compute only net fluxes for each REV following a similar procedure as for the blood fluxes described above. In case of the hybrid model, we compute the net flux in a REV_j by:

$$NF_{\text{cap},\text{t}}^{\text{HY}}(\text{REV}_j) = \frac{\rho_{\text{int}} L_{\text{cap}} S_j}{|\text{REV}_j|} \int_{\text{REV}_j} (p^{\text{t}}(\mathbf{x}) - p^{\text{cap}}(\mathbf{x})) - (\pi_p - \pi_{\text{int}}) d\mathbf{x}.$$

Defining the net inflow flux $NF_{\text{cap},\text{t}}^{\text{HY},\text{in}}(\text{REV}_j)$ and outflow flux $NF_{\text{cap},\text{t}}^{\text{HY},\text{out}}(\text{REV}_j)$ as in the previous cases, the total inflow is given by:

$$MF_{\text{cap},\text{t}}^{\text{HY},\text{in}} = \sum_{j=1}^{N_{\text{REV}}} NF_{\text{cap},\text{t}}^{\text{HY},\text{in}}(\text{REV}_j) \quad (22)$$

and the total outflow is calculated as the sum of the net outflows.

For the fully-discrete model, we compute the net flow in REV_j as follows:

$$NF_{\text{cap},\text{t}}^{\text{FD}}(\text{REV}_j) = \rho_{\text{int}} \cdot 2\pi L_{\text{cap}} \sum_{k \in \Lambda_{\text{C},j}} R_k \int_{\Lambda_k} (\bar{p}^{\text{t}} - p^{\text{v}}) - (\pi_p - \pi_{\text{int}}) dS.$$

As in this case of the hybrid model, the total inflow is given as in (22). Having these definitions at hand, we first compute the mass fluxes for the FD-model. Using these values, we determine the values of the parameter α in (11) such that the following objective functions are minimized:

$$f_1(\alpha) = \sqrt{\sum_{\beta} \sum_{\gamma} \frac{1}{2} \left(MF_{\beta,\gamma}^{\text{HY}} - MF_{\beta,\gamma}^{\text{FD}} \right)^2},$$

for $\beta \in \{\text{LV}, \text{cap}\}$ and $\gamma \in \{\text{in}, \text{out}\}$, and

$$f_2(\alpha) = \sqrt{\frac{1}{2} \left(MF_{\text{LV},\text{in}}^{\text{HY}} - MF_{\text{LV},\text{in}}^{\text{FD}} \right)^2}.$$

The results obtained with the hybrid model strongly depend on the value of α in (11), as we can deduce from Fig. 10, where both objective functions f_1 and f_2 are plotted with respect to the parameter α . For the objective function f_2 , it is easy to identify the minimum at $\alpha = 0.4$, while for f_1 the minimum is attained at $\alpha = 0.46$. The choice between these two values of α is made comparing the fluxes listed in Table 2, where we report the fluxes obtained on the finest level for both the fully-discrete (FD) and the hybrid (HY) models (details to the mesh refinements are postponed to Section 4.4). The results for the latter one are provided for $\alpha \in \{0.2, 0.4, 0.46, 0.9\}$. We can observe a good agreement between the hybrid and the fully-discrete models, in particular with respect to the inflow due to the larger vessels, if $\alpha = 0.4$ is chosen. The major differences in the fluxes consist in the contributions of the homogenized capillaries. In fact, using the hybrid model, the mass fluxes into the capillary continuum and out of

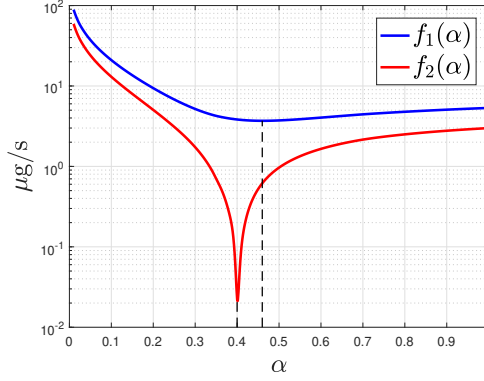


Figure 10: Graphs of the objective functions f_1 and f_2 . For f_1 , the minimum is reached at $\alpha = 0.46$, while, for f_2 it can be seen at a first glance that the minimum is attained at $\alpha = 0.4$.

the capillary continuum are significantly overestimated than those of the fully-discrete model. On the other hand, choosing $\alpha = 0.46$ yields an overall better agreement with the fully-discrete model, because all four fluxes are optimized at the same time, but not a single quantity is as good approximated as for $\alpha = 0.4$. Moreover, due to the fact that in a small neighbourhood of the the minimum, the function f_1 is relatively flat, the difference between $|f_1(0.4) - f_1(0.46)|$ is about $0.141 \mu\text{g/s}$. For completeness, we report the fluxes for $\alpha = 0.2$ and $\alpha = 0.9$ as well to shown by how much these results differ from the solution of the fully-discrete model. Therefore, for the rest of the paper, we proceed comparing the fully-discrete model with the hybrid model, where we fixed $\alpha = 0.4$ in (11).

Lastly, to validate the numerical discretization of the hybrid model, we report in Fig. 11 the numerical mass fluxes, where each plot of the flux is calculated with respect to the mesh refinement. It can be seen that for all the quantities reported, the curves plotted are approaching asymptotic values, as the mesh is refined. This behavior demonstrates that the mass fluxes obtained at the finest level and reported in Table 2 are representative for the hybrid model.

Table 2: Mass fluxes at the boundaries and interfaces of the vascular system. All the fluxes that are presented in this table are given in $\mu\text{g/s}$. For the hybrid method, the fluxes reported are obtained for different α .

	Large vessels		Capillary bed		Tissue
Method	$MF_{LV,in}$	$MF_{LV,out}$	$MF_{cap,in}$	$MF_{cap,out}$	$MF_{cap,t}$
FD	9.80161	10.4964	1.30573	0.61093	$2.54991 \cdot 10^{-3}$
HY $_{\alpha=0.4}$	9.79829	7.80573	2.04311	4.03567	$1.10565 \cdot 10^{-3}$
HY $_{\alpha=0.46}$	8.89951	7.14353	1.87204	3.62801	$1.04549 \cdot 10^{-3}$
HY $_{\alpha=0.2}$	16.9280	13.2730	2.86975	6.52477	$1.48711 \cdot 10^{-3}$
HY $_{\alpha=0.9}$	5.87650	4.95714	1.17063	2.08998	$0.78677 \cdot 10^{-3}$

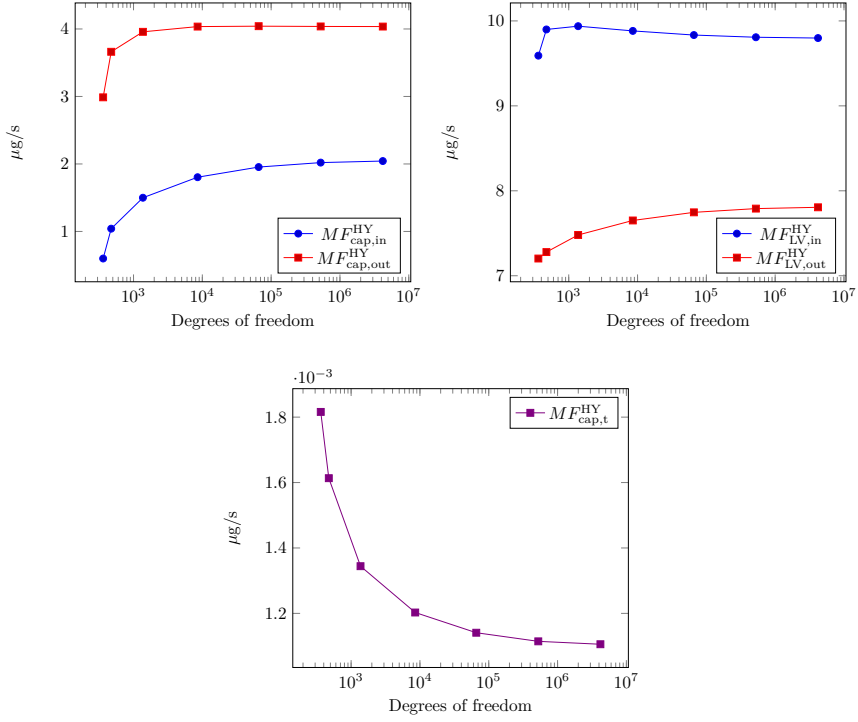


Figure 11: Behavior of the mass fluxes for the hybrid approach with respect to the number of degrees of freedom. At the top, the fluxes at the boundaries of the capillaries and of the large vessels are reported. At the bottom, the total net flux from the capillary bed into the tissue for the hybrid approach is presented.

4.4 Comparison of the REV pressures

After comparing the mass fluxes obtained by the two modeling approaches, we proceed with the comparison of the REV-pressures within the tissue and the capillary bed. For the hybrid model, the averaged pressure $p_{(j),\text{HY}}^{\text{cap}}$ in the capillaries for the REV_j is given by the definition (10), while the average pressure in the tissue is defined as:

$$p_{(j),\text{HY}}^{\text{t}} = \frac{1}{|\text{REV}_j|} \int_{\text{REV}_j} p^{\text{t}}(x) \, dx. \quad (23)$$

In case of the fully-discrete model, we use again (23) to determine the REV-pressure within the tissue and label this value by $p_{(j),\text{FD}}^{\text{t}}$. The REV-pressure for the capillaries with respect to an REV_j is approximated by:

$$p_{(j),\text{FD}}^{\text{cap}} = \frac{1}{|\Lambda_{\text{C},j}|} \int_{\Lambda_{\text{C},j}} p^{\text{v}}(x) \, dx.$$

Furthermore, for the REV_j we define the relative pressure error $E_{\text{r}}^{\text{cap}}$ in the

capillaries and E_r^t in the tissue as:

$$E_r^\beta(j) = \frac{|p_{(j),\text{HY}}^\beta - p_{(j),\text{FD}}^\beta|}{p_{(j),\text{HY}}^\beta}, \quad \beta \in \{\text{cap}, \text{t}\}.$$

The results obtained by means of the hybrid and fully-discrete methods are reported for each REV in Table 3, together with the numeration in the mesh and the center of each REV. The average difference between the pressures obtained with the hybrid method and the fully-discrete method is given by approximately 537.08 Pa (corresponding to 4.03 mmHg) for the capillaries, while the average difference within the tissue is given by approximately 316.27 Pa (corresponding to 2.37 mmHg). These values yield an average relative error of the pressures between the hybrid model and the fully-discrete of approximately $\overline{E_r^{\text{cap}}} = 11.37\%$ in the capillaries and of $\overline{E_r^t} = 13.97\%$ in the tissue.

Table 3: Averaged REV-pressures in the capillaries and in the tissue.

REV		$p_{(j)}^{\text{cap}}$ [Pa]			$p_{(j)}^t$ [Pa]		
j	Center [mm]	HY	FD	E_r^{cap}	HY	FD	E_r^t
1	(0.284, 0.284, 0.542)	5107.77	4535.61	11.20%	2400.12	1972.80	17.80%
2	(0.852, 0.284, 0.542)	5217.07	4704.37	9.83%	2465.14	2027.71	17.74%
3	(0.284, 0.852, 0.542)	5002.77	4658.86	6.87%	2325.75	1961.99	15.64%
4	(0.852, 0.852, 0.542)	5041.25	4447.64	11.77%	2392.00	1939.18	18.93%
5	(0.284, 0.284, 1.623)	4843.99	5465.34	12.83%	2156.06	2469.00	14.51%
6	(0.852, 0.284, 1.623)	5041.86	5425.96	7.62%	2295.94	2440.22	6.28%
7	(0.284, 0.852, 1.623)	3789.44	4637.19	22.37%	1847.50	2192.57	18.68%
8	(0.852, 0.852, 1.623)	4960.14	4539.09	8.49%	2178.97	2132.44	2.14%

Finally, in Table 4 we report the average relative errors $\overline{E_r^{\text{cap}}}$ and $\overline{E_r^t}$ of the hybrid model with mesh refinement. These errors are calculated with respect to the REV-pressures obtained by the fully-discrete model on the finest mesh, i.e., the values reported in Table 3 in the corresponding columns. Table 4 suggests that the errors $\overline{E_r^\beta}$ converge to a fixed value. The remaining error can be considered as the modeling error arising from the homogenization.

If we calculate the solution of the hybrid model on the mesh with $16 \times 16 \times 16$ elements in both the capillaries and tissue for a total of 8538 degrees of freedom, we obtain that the average relative errors differ by less than 1% from the average relative errors on the finest mesh. In this situation, we can assert that the modeling error dominates the discretization error and thus the obtained pressures can be considered as representative for the hybrid model. On the other hand, the relative error for the pressure in the fully-discrete model is already less than 1% on the coarsest mesh, where the elements coincide with the REV's. However, in this case the linear system has still 12995 degrees of freedom in the network and 8 in the tissue. Therefore, compared with the fully-discrete model, a smaller linear system can be solved to obtain representative values for the fluxes and pressures in the hybrid model. This reduction in the number of degrees of freedom is expected to become more sensible, if a larger system is considered.

Table 4: Averaged relative errors of the REV-pressures in the capillaries and in the tissue with respect to the degrees of freedom (dofs).

dofs	$\overline{E}_r^{\text{cap}}$	$\overline{E}_r^{\text{t}}$
362	16.20%	22.30%
474	14.15%	17.70%
1370	12.71%	15.51%
8538	11.95%	14.56%
65882	11.58%	14.17%
524634	11.42%	14.02%
4194650	11.37%	13.97%

4.5 Sensitivity analysis of α for different boundary conditions

In this section, we study the influence of the boundary conditions on the parameter α defined in (11). Considering the results reported in Table 2, one can conclude that the arterioles and venules determine significantly the pressure and velocity fields within the microvascular system. Therefore we vary the pressures at the boundary of these vessels as follows. Let us denote by \bar{p}_a and \bar{p}_v the average boundary pressure of the arterioles and of the venules, respectively. For the experiment setting considered here, the difference

$$\delta = |\bar{p}_v - \bar{p}_a|$$

amounts to approximately 5000 Pa (corresponding to 37.5 mmHg). For all

$$i \in \{-10\%, \dots, -1\%, 0\%, 1\%, \dots, 10\%\},$$

we add the pressure $\frac{1}{2}\delta \cdot i$ to each boundary node corresponding to an arteriole, while at the venous boundary nodes, we subtract the same quantity. This yields a variation in the average pressure difference by the fraction i of δ . For each new network, the optimization process described in Section 4.3 is conducted and the resulting graphs of the objective functions f_1 and f_2 have the same shape as in Fig. 10. Following the same strategy described above, only the optimal α for the objective function f_2 is considered and reported in Table 5.

If the average pressure difference is reduced, the optimal α is subject to relatively small variations. On the other hand, if δ becomes larger, the deviations from $\alpha = 0.4$ become larger. However, as we can observe in Fig. 10, a small deviation from the optimal α yields a sensible difference in the flux $MF_{\text{LV},\text{in}}$. Therefore, a single α cannot be determined in advance and used for other samples with different data, but the calibration of α has to be repeated for every new experimental setting.

5 Concluding remarks

In this work, we have presented a hybrid model for simulating blood flow through networks at the level of microcirculation. The presented model is based on 1D

Table 5: Optimal α values for the cases, in which the average pressure difference δ is varied by the percentage i .

i [%]	α
-10, -9 - 8 - 7, -6, -4, -3, -2	0.41
-5	0.42
-1, 0, +1	0.4
+2	0.38
+3, +4	0.39
+5, +6, +7	0.37
+8, +9, +10	0.36

flow models for the larger vessels and on homogenization techniques for the capillaries and the tissue. Thereby, the capillaries and the tissue are modeled as 3D coupled porous media resulting in a double 3D continua approach for simulating flows within both systems. In order to validate the simulation results obtained by our hybrid model, we have generated a reference solution by means of a fully-discrete 3D-1D coupled model. Here, the complete vascular network is resolved by 1D flow models and only the flow within the tissue is considered as a porous medium flow.

For the comparison criteria between the two models, we have chosen mass fluxes at the boundaries of the microvascular system and averaged pressures for each REV. If the parameter α in (11) is chosen appropriately, our simulation results showed that the fluxes at the inlet and outlets of the larger vessels obtained with our hybrid model coincide in a satisfactory manner with the corresponding fluxes obtained solving the fully-discrete model. On the other hand, the fluxes through the capillaries are overestimated by the hybrid model. Furthermore the net mass flux between the tissue and the capillaries is approximately 2.3 times higher for the fully-discrete model than for the hybrid model. Regarding the averaged pressures for each REV, the simulations showed that the pressures obtained with the hybrid model differ, in average, by approximately 4 mmHg in the capillaries and by approximately 2.37 mmHg in the tissue from the solution of the fully-discrete model. A more thorough comparison with respect to the reduction of the computational cost will be subject of future work. For this purpose, a larger tissue sample should be examined. Additionally, we investigated the influence of different boundary conditions on the optimal parameter α . Despite the fact that α varies only slightly, the results suggest that it may be necessary to calibrate α for every experimental setting to obtain accurate approximations of the mass fluxes provided by the fully-discrete model. Similarly, in [49] a parameter has to be optimized as well to model the flux between the different vessel types. These observations suggest that in context of hybrid models for microvasculature different unknown parameters occur, whose value is not known a priori. As a consequence, further investigations are required to improve the hybrid modeling approach. In particular, it would be of great interest to determine, if a combination of such parameters exists that can be applied to different settings and provides accurate results.

Considering other works regarding upscaling of capillary structures, such as [40], we obtained comparable results. In [40], the authors obtained perme-

abilities in the order of 10^{-14} m^2 , i.e., approximately 5 times larger values than the ones depicted in Fig. 9. However, having a closer look to the data, one can observe that in [40] the radius of the capillaries is around $3 \text{ }\mu\text{m}$, while in our experiment the radius of the capillaries ranges between $1.6 \text{ }\mu\text{m}$ and $7 \text{ }\mu\text{m}$, which explains the difference. Regarding the choice of the parameter R_T , the threshold $7 \text{ }\mu\text{m}$ is in good agreement with the morphological values listed in [16, Table 1].

A limitation of our hybrid model consists in the determination of the parameter α . In this paper, we employed the solution of the fully-discrete model to tune the parameter α in order to optimize certain fluxes. A way to make a more independent definition of α may involve a precise computation of the quantities $K_v^{(j)}$ and $\ell_c^{(kj)}$ in (10). Furthermore, a better approximation of the permeabilities of the homogenized system may be necessary, in particular, if larger systems are considered. We also point out that the hybrid model we presented allows one to compute only net fluxes.

A clear advantage of the hybrid model is the fact that only meso-scale data are required to parametrize the model, whereas micro-scale data are necessary for fully discrete models. This holds for boundary data as well as for model parameters. Furthermore, we have provided tools to analyze homogenized models systematically that can be used to verify other upscaling strategies.

Future work in this field might be concentrated on coupling the new hybrid model for blood flow with transport models for therapeutic agents and other substances such that cancer therapies like hyperthermia can be simulated. A further interesting issue that could be studied by means of the hybrid model is to enhance existing flow models for whole organs or part of organs such that the diagnosis techniques for clinical

Acknowledgment

This work was partially supported by the Cluster of Excellence in Simulation Technology (EXC 310/2) and the DFG grant (WO/671 11-1). We gratefully acknowledge the authors of [45] and, in particular, Prof. Bruno Weber and Prof. Patrick Jenny, for providing the data set to the vascular network considered in this paper.

References

- [1] J. Bear. *Dynamics of fluids in porous media*. Courier Corporation, 2013.
- [2] M. Blatt and P. Bastian. The iterative solver template library. In *International Workshop on Applied Parallel Computing*, pages 666–675. Springer, 2006.
- [3] Markus Blatt and Peter Bastian. The iterative solver template library. In *International Workshop on Applied Parallel Computing*, pages 666–675. Springer, 2006.
- [4] Markus Blatt and Peter Bastian. On the generic parallelisation of iterative solvers for the finite element method. *International Journal of Computational Science and Engineering*, 4(1):56–69, 2008.

- [5] Markus Blatt, Ansgar Burchardt, Andreas Dedner, Christian Engwer, Jorrit Fahlke, Bernd Flemisch, Christoph Gersbacher, Carsten Gräser, Felix Gruber, Christoph Grüninger, et al. The distributed and unified numerics environment, version 2.4. *Archive of Numerical Software*, 4(100):13–29, 2016.
- [6] D. Boas, S. Jones, A. Devor, T. Huppert, and A. Dale. A vascular anatomical network model of the spatio-temporal response to brain activation. *Neuroimage*, 40(3):1116–1129, 2008.
- [7] Carina Bringedal, Inga Berre, Iuliu Sorin Pop, and Florin A Radu. Upscaling of nonisothermal reactive porous media flow under dominant péclet number: the effect of changing porosity. *Multiscale Modeling & Simulation*, 14(1):502–533, 2016.
- [8] L. Cattaneo and P. Zunino. A computational model of drug delivery through microcirculation to compare different tumor treatments. *International journal for numerical methods in biomedical engineering*, 30(11):1347–1371, 2014.
- [9] C. D’Angelo. *Multi scale modelling of metabolism and transport phenomena in living tissues*, PhD Thesis. EPFL, Lausanne, 2007.
- [10] C. D’Angelo. Finite element approximation of elliptic problems with dirac measure terms in weighted spaces: applications to one-and three-dimensional coupled problems. *SIAM Journal on Numerical Analysis*, 50(1):194–215, 2012.
- [11] C. D’Angelo and A. Quarteroni. On the coupling of 1d and 3d diffusion-reaction equations: application to tissue perfusion problems. *Mathematical Models and Methods in Applied Sciences*, 18(08):1481–1504, 2008.
- [12] A. Despopoulos and S. Silbernagl. *Color atlas of physiology*. Thieme, 2003.
- [13] M. Dewhirst and T. Secomb. Transport of drugs from blood vessels to tumour tissue. *Nature Reviews Cancer*, 17(12):738, 2017.
- [14] Peter Dietrich, Rainer Helmig, Martin Sauter, Heinz Hötzl, Jürgen Köngeter, and Georg Teutsch. *Flow and transport in fractured porous media*. Springer Science & Business Media, 2005.
- [15] W. El-Bouri and S. Payne. Multi-scale homogenization of blood flow in 3-dimensional human cerebral microvascular networks. *Journal of theoretical biology*, 380:40–47, 2015.
- [16] W. El-Bouri and S. Payne. Investigating the effects of a penetrating vessel occlusion with a multi-scale microvasculature model of the human cerebral cortex. *NeuroImage*, 172:94–106, 2018.
- [17] K. Erbertseder, J. Reichold, B. Flemisch, P. Jenny, and R. Helmig. A coupled discrete/continuum model for describing cancer-therapeutic transport in the lung. *PLoS One*, 7(3):e31966, 2012.

- [18] R. Fahraeus and T. Lindqvist. The viscosity of the blood in narrow capillary tubes. *American Journal of Physiology-Legacy Content*, 96(3):562–568, 1931.
- [19] L. Formaggia, A. Quarteroni, and A. Veneziani. *Cardiovascular Mathematics: Modeling and simulation of the circulatory system*, volume 1. Springer Science & Business Media, 2010.
- [20] Luca Formaggia, Fabio Nobile, Alfio Quarteroni, and Alessandro Veneziani. Multiscale modelling of the circulatory system: a preliminary analysis. *Computing and visualization in science*, 2(2-3):75–83, 1999.
- [21] Y. Fung and B. Zweifach. Microcirculation: mechanics of blood flow in capillaries. *Annual Review of Fluid Mechanics*, 3(1):189–210, 1971.
- [22] Ingeborg G Gjerde, Kundan Kumar, Jan M Nordbotten, and Barbara Wohlmuth. Splitting method for elliptic equations with line sources. *arXiv preprint arXiv:1810.12979*, 2018.
- [23] Simone di Gregorio, Luca Possenti, Simone di Gregorio, Fannie Maria Gerosa, Giorgio Raimondi, Giustina Casagrande, Maria Laura Costantino, and Paolo Zunino. A computational model for microcirculation including fahraeus-lindqvist effect, plasma skimming and fluid exchange with the tissue interstitium. *International Journal for Numerical Methods in Biomedical Engineering*, 2018.
- [24] R. Helmig. *Multiphase flow and transport processes in the subsurface: a contribution to the modeling of hydrosystems*. Springer-Verlag, 1997.
- [25] K. Holter, B. Kehlet, A. Devor, T. Sejnowski, A. Dale, S. Omholt, O. Ottersen, E. Nagelhus, K. Mardal, and K. Pettersen. Interstitial solute transport in 3d reconstructed neuropil occurs by diffusion rather than bulk flow. *Proceedings of the National Academy of Sciences*, page 201706942, 2017.
- [26] Richard Hsu and Timothy W Secomb. A green’s function method for analysis of oxygen delivery to tissue by microvascular networks. *Mathematical biosciences*, 96(1):61–78, 1989.
- [27] Y. Iturria-Medina, R. Sotero, P. Toussaint, J. Mateos-Pérez, A. Evans, M. Weiner, P. Aisen, R. Petersen, C. Jack, W. Jagust, et al. Early role of vascular dysregulation on late-onset alzheimer’s disease based on multifactorial data-driven analysis. *Nature communications*, 7:11934, 2016.
- [28] A. Khaled and K. Vafai. The role of porous media in modeling flow and heat transfer in biological tissues. *International Journal of Heat and Mass Transfer*, 46(26):4989–5003, 2003.
- [29] T. Köppl, E. Vidotto, and B. Wohlmuth. A local error estimate for the poisson equation with a line source term. In *Numerical Mathematics and Advanced Applications ENUMATH 2015*, pages 421–429. Springer, 2016.
- [30] T. Köppl, E. Vidotto, B. Wohlmuth, and P. Zunino. Mathematical modeling, analysis and numerical approximation of second-order elliptic problems with inclusions. *Mathematical Models and Methods in Applied Sciences*, 28(05):953–978, 2018.

- [31] Tobias Köppl, Ettore Vidotto, and Barbara Wohlmuth. A local error estimate for the poisson equation with a line source term. In *Numerical Mathematics and Advanced Applications ENUMATH 2015*, pages 421–429. Springer, 2016.
- [32] J Rodney Levick and C Charles Michel. Microvascular fluid exchange and the revised starling principle. *Cardiovascular research*, 87(2):198–210, 2010.
- [33] JR Levick. Capillary filtration-absorption balance reconsidered in light of dynamic extravascular factors. *Exp Physiol*, 76(6):825–857, 1991.
- [34] S. Mahjoob and K. Vafai. Analytical characterization of heat transport through biological media incorporating hyperthermia treatment. *International Journal of Heat and Mass Transfer*, 52(5-6):1608–1618, 2009.
- [35] Anastasios Matzavinos and Mariya Ptashnyk. Homogenization of oxygen transport in biological tissues. *Applicable Analysis*, 95(5):1013–1049, 2016.
- [36] M. Nabil and P. Zunino. A computational study of cancer hyperthermia based on vascular magnetic nanoconstructs. *Royal Society open science*, 3(9):160287, 2016.
- [37] D. Notaro, L. Cattaneo, L. Formaggia, A. Scotti, and P. Zunino. A mixed finite element method for modeling the fluid exchange between microcirculation and tissue interstitium. In *Advances in Discretization Methods*, pages 3–25. Springer, 2016.
- [38] R. Penta, D. Ambrosi, and A. Quarteroni. Multiscale homogenization for fluid and drug transport in vascularized malignant tissues. *Mathematical Models and Methods in Applied Sciences*, 25(01):79–108, 2015.
- [39] A. Petryk, A. Giustini, R. Gottesman, P. Kaufman, and P. Hoopes. Magnetic nanoparticle hyperthermia enhancement of cisplatin chemotherapy cancer treatment. *International Journal of Hyperthermia*, 29(8):845–851, 2013.
- [40] M. Peyrounette, Y. Davit, M. Quintard, and S. Lorthois. Multiscale modelling of blood flow in cerebral microcirculation: Details at capillary scale control accuracy at the level of the cortex. *PloS one*, 13(1):e0189474, 2018.
- [41] A. Pries and T. Secomb. Making microvascular networks work: angiogenesis, remodeling, and pruning. *Physiology*, 29(6):446–455, 2014.
- [42] A. Pries, T. Secomb, and P. Gaehtgens. Biophysical aspects of blood flow in the microvasculature. *Cardiovascular research*, 32(4):654–667, 1996.
- [43] A. Pries, T. Secomb, P. Gaehtgens, and J. Gross. Blood flow in microvascular networks. experiments and simulation. *Circulation research*, 67(4):826–834, 1990.
- [44] Alfio Quarteroni and Luca Formaggia. Mathematical modelling and numerical simulation of the cardiovascular system. *Handbook of numerical analysis*, 12:3–127, 2004.

- [45] J. Reichold, M. Stampanoni, A. L. Keller, A. Buck, P. Jenny, and B. Weber. Vascular graph model to simulate the cerebral blood flow in realistic vascular networks. *Journal of Cerebral Blood Flow & Metabolism*, 29(8):1429–1443, 2009.
- [46] Philippe Renard, Gaëlle Le Loc’h, Emmanuel Ledoux, Ghislain de Marsily, and Rae Mackay. A fast algorithm for the estimation of the equivalent hydraulic conductivity of heterogeneous media. *Water Resources Research*, 36(12):3567–3580, 2000.
- [47] T. Roose and M. Swartz. Multiscale modeling of lymphatic drainage from tissues using homogenization theory. *Journal of biomechanics*, 45(1):107–115, 2012.
- [48] R. Shipley and S. Chapman. Multiscale modelling of fluid and drug transport in vascular tumours. *Bulletin of mathematical biology*, 72(6):1464–1491, 2010.
- [49] RJ Shipley, AF Smith, PW Sweeney, AR Pries, and TW Secomb. A hybrid discrete-continuum approach for modelling microcirculatory blood flow. *Mathematical medicine and biology: a journal of the IMA*, 2019.
- [50] S. Stacker and M. Achen. Emerging roles for vegf-d in human disease. *Biomolecules*, 8(1):1, 2018.
- [51] E. H. Starling. On the absorption of fluids from the connective tissue spaces. *The Journal of physiology*, 19(4):312–326, 1896.
- [52] Karen H Støverud, Melanie Darcis, Rainer Helmig, and S Majid Hasanizadeh. Modeling concentration distribution and deformation during convection-enhanced drug delivery into brain tissue. *Transport in porous media*, 92(1):119–143, 2012.
- [53] Yuanliang Tang and Ying He. Numerical modeling of fluid and oxygen exchanges through microcirculation for the assessment of microcirculation alterations caused by type 2 diabetes. *Microvascular research*, 117:61–73, 2018.
- [54] F. Waterman, L. Tupchong, R. Nerlinger, and J. Matthews. Blood flow in human tumors during local hyperthermia. *International Journal of Radiation Oncology* Biology* Physics*, 20(6):1255–1262, 1991.